VIROLOGY

Structural basis for HCMV Pentamer receptor recognition and antibody neutralization

Marc Kschonsak[1]*†, Matthew C. Johnson[1]†, Rachel Schelling[2], Evan M. Green[1], Lionel Rougé[1], Hoangdung Ho[1], Nidhi Patel[1], Cem Kilic[3], Edward Kraft[4], Christopher P. Arthur[1], Alexis L. Rohou[1], Laetitia Comps-Agrar[3], Nadia Martinez-Martin[5]‡, Laurent Perez[2]*, Jian Payandeh[1]*§, Claudio Ciferri[1]*

Human cytomegalovirus (HCMV) represents the viral leading cause of congenital birth defects and uses the gH/gL/UL128-130-131A complex (Pentamer) to enter different cell types, including epithelial and endothelial cells. Upon infection, Pentamer elicits the most potent neutralizing response against HCMV, representing a key vaccine candidate. Despite its relevance, the structural basis for Pentamer receptor recognition and antibody neutralization is largely unknown. Here, we determine the structures of Pentamer bound to neuropilin 2 (NRP2) and a set of potent neutralizing antibodies against HCMV. Moreover, we identify thrombomodulin (THBD) as a functional HCMV receptor and determine the structures of the Pentamer-THBD complex. Unexpectedly, both NRP2 and THBD also promote dimerization of Pentamer. Our results provide a framework for understanding HCMV receptor engagement, cell entry, antibody neutralization, and outline strategies for antiviral therapies against HCMV.

INTRODUCTION

Human cytomegalovirus (HCMV) is a member of the betaherpesvirus family, responsible for severe morbidity and mortality in immunocompromised individuals (*1*). HCMV infection is particularly threatening during pregnancy and represents the viral leading cause of congenital birth defects (*2*). HCMV exhibits a broad cellular tropism and uses the Pentamer complex to bind to different receptor proteins and infect diverse cell types including epithelial, endothelial, and myeloid cells (*3*–*6*). HCMV receptor binding is thought to provide the triggering signal for the gB glycoprotein to catalyze membrane fusion between virus and host cells, allowing HCMV to enter cells, replicate, and establish its latency (*7*). Neuropilin 2 (NRP2) deficiency has been demonstrated to make endothelial and epithelial cells resistant to HCMV infection, indicating a key role of NRP2 as an HCMV receptor (*5*), but the structural basis for this interaction has remained unknown. HCMV Pentamer also binds to thrombomodulin (THBD) with nanomolar affinity, but a role for THBD in the entry of HCMV has remained enigmatic (*5*).

Upon infection, HCMV elicits extremely potent neutralizing antibodies against the Pentamer, underlining the importance of this complex as a therapeutic target and vaccine candidate against HCMV (*8*). Despite considerable efforts, a vaccine against HCMV still represents an unmet medical need, and no approved therapy is currently available to treat congenital HCMV infection (*9*, *10*). This gap is largely due to the lack of a structural understanding of the interaction between HCMV Pentamer and host cellular receptors, and our limited knowledge of the epitopes relevant for HCMV Pentamer neutralization.

In this study, we determined high-resolution structures of HCMV Pentamer in complex with the cellular receptors NRP2 and THBD. These structures highlight the specific interactions required for HCMV Pentamer–receptor recognition and reveal an unanticipated dimerization of the Pentamer-receptor complexes. We found that the interaction between Pentamer and NRP2 or THBD is mutually exclusive, and both are functional receptors mediating entry into different cell types, rather than being co-receptors. We also report the structures of Pentamer bound to a set of potent neutralizing antibodies that identify key neutralizing sites against HCMV. Our studies provide a framework for understanding HCMV receptor recognition and antibody-based neutralization and will serve as a template for therapeutic development against HCMV.

RESULTS

Structural basis for Pentamer-NRP2 receptor binding

Previous structural studies of HCMV glycoprotein complexes have indicated that these molecules are refractory to high-resolution structure determination due to their inherent flexibility, elongated nature, and the numerous glycosylation sites (*11*). We therefore reconstituted HCMV Pentamer in complex with the soluble ectodomain of NRP2 and the neutralizing Fabs 13H11 and 8I21, and used single-particle cryo–electron microscopy (cryo-EM) to determine their structure (Fig. 1 and fig. S1). Two-dimensional (2D) class averaging identified two particle populations: one monomeric, representing most of the particles in which one Pentamer was bound to one copy of NRP2, and a second unexpected dimeric population in which two Pentamer complexes were wrapped around a single NRP2 molecule and arranged in a head-to-head fashion (fig. S1, D and F).

The structure of the monomeric Pentamer-NRP2 complex bound to 13H11 and 8I21 was determined to a resolution of ~3.1 Å (fig. S1, G to I). Focused 3D reconstructions allowed us to build a structural model for most of the HCMV Pentamer–13H11–8I21

[1]Department of Structural Biology, Genentech Inc., South San Francisco, CA 94080, USA. [2]University of Lausanne (UNIL), Lausanne University Hospital (CHUV), Department of Medicine, Division of Immunology and Allergy, Center for Human Immunology (CHIL), Lausanne, Switzerland. [3]Department of Biochemical and Cellular Pharmacology, Genentech Inc., South San Francisco, CA 94080, USA. [4]Department of Biomolecular Resources, Genentech Inc., South San Francisco, CA 94080, USA. [5]Department of Microchemistry, Proteomics and Lipidomics, Genentech Inc, South San Francisco, CA 94080, USA.
*Corresponding author. Email: ciferri.claudio@gene.com (C.C.); kschonsak.marc@gene.com (M.K.); Laurent.Perez@chuv.ch (L.P.); jpayandeh@interlinetx.com (J.P.)
†These authors contributed equally to this work.
‡Present address: Regeneron, Tarrytown, New York, NY, USA.
§Present address: Department of Proteomics and Bioinformatics, Interline Therapeutics, South San Francisco, CA 94080, USA.

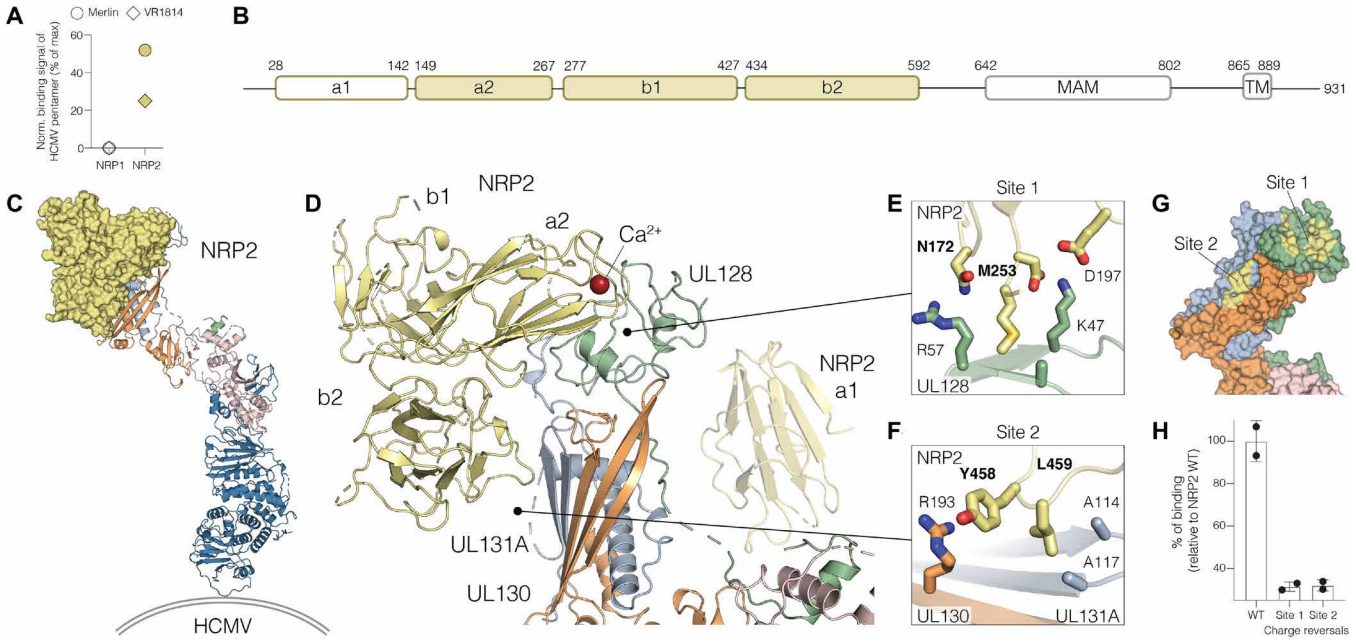

Fig. 1. Structure of HCMV Pentamer gHgLUL128-131A bound to NRP2. (**A**) HCMV Pentamer from two different strains (Merlin and VR1814) selectively a interacts with NRP2 and not NRP1, as previously described (*5*). (**B**) Schematic domain organization of human NRP2. (**C**) Front view of HCMV Pentamer complex (shown in ribbon) bound to NRP2 a2b1b2 domains (shown in surface representation). Fabs are not rendered for clarity. (**D**) Close-in view of HCMV Pentamer distal region showing NRP2 a1a2b1b2 domains, UL128-131A, gL, and the gH N terminus. NRP2 a1 appears to interact loosely with HCMV Pentamer, is not well resolved in the cryo-EM map, and is not modeled in the structure. Fabs are not rendered for clarity. (**E**) Close-in view of HCMV Pentamer distal region as described in (D) with highlighted sites of interaction between Pentamer and NRP2 a2 domain (site 1). Residues in bold represent reverse-charge mutations. (**F**) Close-in view of HCMV Pentamer distal region as described in (D) with highlighted sites of interaction between Pentamer and NRP2 b2 domain (site 2). Residues in bold represent reverse-charge mutations. (**G**) Close-in view of HCMV Pentamer distal region as described in (D) with highlighted surface interaction area to NRP2. (**H**) Summarized binding affinities of Pentamer to NRP2 WT or single-site point mutations (site 1: N172R, M253E, and A254E; site 2: Y458R and L459R). Kinetic parameters are representative of two independent assays.

complex and the NRP2 a2, b1, and b2 domains (Fig. 1, C and D; fig. S2A; and table S1). The density for the a1 domain of NRP2 was weaker than the remaining part of the complex, presumably due to flexibility or to the ability of a1 domain to loosely interact with the Pentamer in different orientations (Fig. 1D and fig. S1G). No density was observed for the C-terminal MAM domain of NRP2, despite its presence in our protein construct and sample.

Three main sites of interaction between NRP2 and the Pentamer were identified, in agreement with recent observations (Fig. 1, E to G) (*12*). At site 1, a calcium-coordinating region in the a2 domain of NRP2 establishes charge interactions with residues localized in the N-terminal domain of UL128 of the Pentamer (Fig. 1, E and G). Specifically, NRP2-D197 and NRP2-D252 interact with UL128-K47, while NRP2-N172 contacts UL128-R57 (Fig. 1E). Site 2 is established between the b2 domain of NRP2 and the C-terminal strand of UL130 and UL131A (Fig. 1, F and G). Notably, we find that charge reversal mutations on Pentamer at either site 1 or 2 disrupted NRP2 binding (Fig. 1H). Relative to unbound NRP2 structures, the a1 domain becomes displaced from the a2b1b2 core upon Pentamer binding and is repositioned to a third site of interaction, site 3, housed along a concave surface of the UL components at the site of attachment between UL128 and gL (Fig. 1D). This region was poorly resolved in our cryo-EM map, suggesting that a1 domain binding to monomeric Pentamer is dynamic, consistent with the finding that NRP2 is still able to interact with Pentamer in the absence of the a1 domain, albeit to a lower degree (*12*).

Although the folds of NRP1 and NRP2 are conserved, the sites of NRP2 interaction with HCMV Pentamer are divergent in NRP1, which provides a structural rationale for the specificity of the NRP2 receptor (fig. S3, A to C). NRP1 and NRP2 proteins are known to interact with several common partners, including vascular endothelial growth factor (VEGF) and the spike protein of severe acute respiratory syndrome coronavirus-2 (SARS-CoV-2), through a mode in which their respective b1 domains interact with a [R/K]XX[R/K] (CendR) motif in the binding partner (*13*, *14*). However, our structure and studies from the McLellan's group (*12*) unambiguously demonstrate that the interaction between Pentamer and NRP2 does not involve this common binding surface on the b1 domain but rather requires specific interactions between the a2 and b2 domains of NRP2 and the UL components of the Pentamer, and in particular UL128 and UL131A (Fig. 1, E to G, and fig. S3D). These features highlight the structural economy underlying the diverse array of cellular proteins with which Pentamer can interact.

The NRP2 receptor interaction with Pentamer may propagate a conformational change to enable or disable binding of other HCMV glycoproteins, such as the prefusion gB. We compared our cryo-EM structure of Pentamer bound to NRP2 with the previously determined crystal structure of Pentamer in the absence of a receptor [Protein Data Bank (PDB): 5VOB; (*15*)] and the structure of the HCMV gHgLgO Trimer [gH and gL subunits only; (*16*)]. Notably, and in agreement with previous findings (*12*), very similar conformations of gH/gL are observed across all comparisons (fig. S4, A and B),

implying that a different mechanism must underlie the activation of the HCMV fusion machinery, as discussed below.

Structural basis for Pentamer-THBD receptor binding

We next reconstituted a stoichiometric complex of the soluble THBD ectodomain with HCMV Pentamer and Fabs 13H11 and MSL-109 and determined this structure to an overall resolution of ~3.3 Å (Fig. 2; figs. S2B and S5, A to F; and table S1). Reminiscent of the NRP2 head-to-head Pentamer dimer population, 2D classification revealed two Pentamer molecules wrapped around one THBD receptor in a head-to-head fashion interacting through the UL128 subunit (Fig. 2B). In this dimeric complex structure, the THBD N-terminal lectin-like domain is sandwiched in between two Pentamer molecules and, specifically, wedged in between the two concave surfaces formed by the UL components at the site of interaction between UL128 and gL (Fig. 2B). We observed additional low-resolution density in the direction of the anchoring point of the receptor on the host cell membrane, likely corresponding to the THBD TME1 and the linker region connecting it to the THBD lectin–like domain on the convex surface of the Pentamer formed by the UL130 and UL131A subunits (fig. S6A). Binding of THBD did not induce any major structural rearrangement of the Pentamer (fig. S4D), as observed for the NRP2-Pentamer complex (fig. S4C).

The THBD lectin–like domain is a globular domain composed of six β strands (b1 to b6) and two α helices (a1 and a2) inserted between b2 and b3 (fig. S6B). Two opposite surfaces of THBD are recognized by the same regions of the two engaging Pentamer molecules, uncovering a marked structural plasticity of this interface (Fig. 2B). Specifically, the N-terminal region of UL128 (UL128-R42 or UL128-Y44) interacts with either THBD-R83 and THBD-E154 or THBD-A123 and THBD-L125, respectively (Fig. 2B). Similarly, the hairpin of UL130 centered at residues UL130-Y169 interacts on one side with THBD-S149 and on the other side with THBD-C133 (Fig. 2B). In addition, the C-terminal region of Pentamer 1 UL128 (UL128-R131, UL128-N134, and UL128-Y137) interacts with THBD-V66 and THBD-D69, while a distinct region on Pentamer 2 UL128 (UL128-R158, UL128-R163, and UL128-Y168) contacts THBD-S49 and THBD-D53 (Fig. 2B). Overall, this structure reveals an unexpectedly large and polyspecific interaction footprint between THBD and a Pentamer dimer at overlapping regions on the UL128 and UL130 subunits (Fig. 2, C and D).

THBD is a functional receptor for HCMV and competes with NRP2 for Pentamer binding

To determine whether THBD is a functional receptor for HCMV, we tested the ability of soluble proteins and antibodies to inhibit

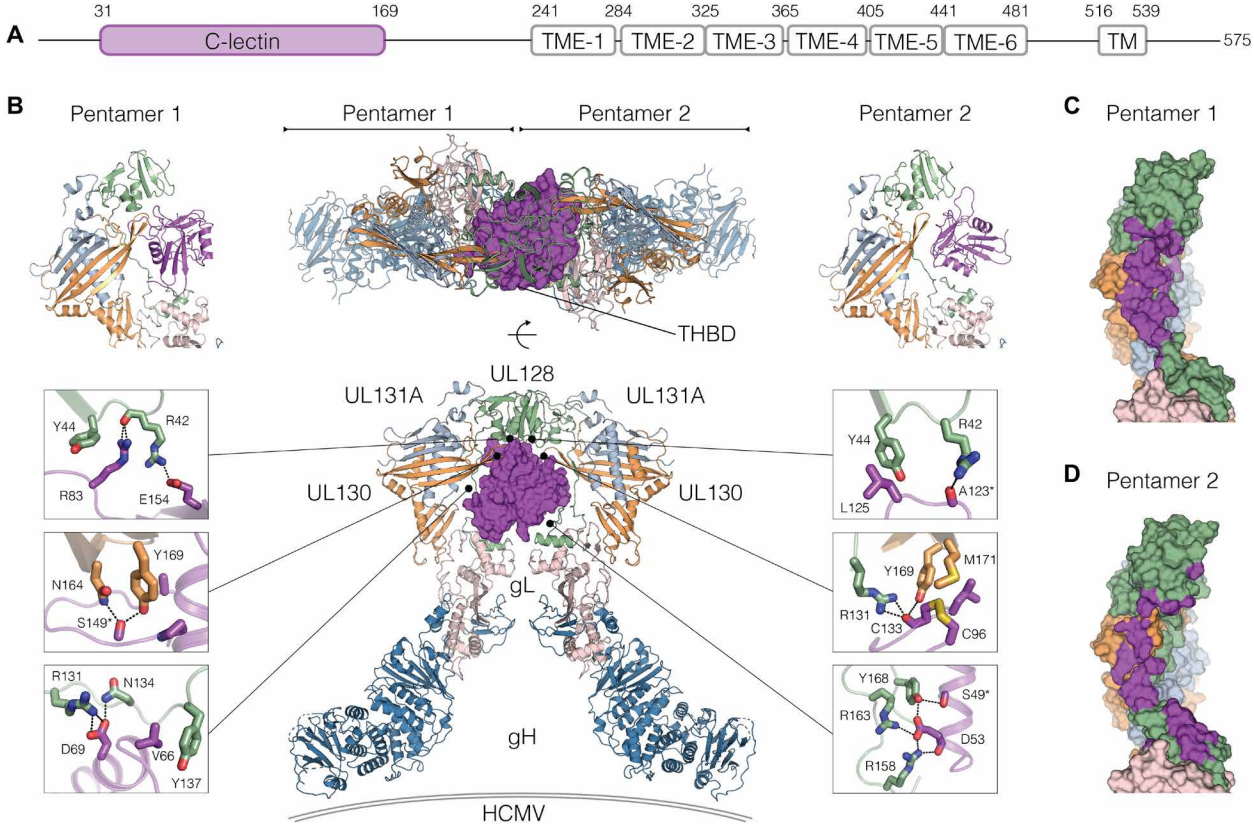

Fig. 2. Structure of HCMV Pentamer gHgLUL128-131A bound to THBD. (**A**) Schematic domain organization of human THBD. (**B**) Top and front view of dimeric HCMV Pentamer complex (shown in ribbon) bound to THBD lectin domain (shown in surface representation). Close-in view of HCMV Pentamer 1 distal region showing THBD lectin domains, UL128-131A, and gL with highlighted sites of interaction between Pentamer 1 and THBD lectin domain. Close-in view of HCMV Pentamer 2 distal region showing THBD lectin domains, UL128-131A, and gL with highlighted sites of interaction between Pentamer 2 and THBD lectin domain. (**C**) Close-in view of HCMV Pentamer 1 distal region as described in (C) with highlighted surface interaction area to THBD. (**D**) Close-in view of HCMV Pentamer 2 distal region as described in (D) with highlighted surface interaction area to THBD.

viral entry in epithelial and endothelial cells. As expected, recombinant NRP2 and a pan-NRP antibody (*17*) inhibited HCMV infection in epithelial and endothelial cells in a dose-dependent manner (Fig. 3A) (*5*). Recombinant THBD reduced viral infection to a much lower extent, but a combination of recombinant THBD and NRP2 inhibited HCMV entry to higher levels than NRP2 alone, suggesting a potential functional role for THBD in HCMV infection (Fig. 3A), and in agreement with our published results (*5*). To further test this hypothesis, we examined the ability of THBD to mediate HCMV entry in cells lacking NRP2 (Fig. 3B and fig. S7A). THBD overexpression had minimal effect on HCMV infection of HAP-1 wild type (WT), but its overexpression in the NRP2 knockout (KO) cells markedly increased viral entry (Fig. 3B and fig. S7, A and B). As a control, we repeated the experiment in the presence of 8I21 monoclonal antibody (mAb) at 0.1 μg/ml. Addition of the pentamer-specific mAb completely abolishes infection, confirming a Pentamer-specific infection (Fig. 3B). Moreover, we observed that THBD-expressing cells were able to spread the virus (fig. S7C). Together, our data indicate that both NRP2 and THBD are relevant receptors for HCMV that may function as independent receptors or co-receptors.

Our structural analyses suggest how the Pentamer has evolved to engage architecturally distinct receptors localized on the surface of different cells. Notably, NRP2 and THBD bind to the Pentamer through unique interaction surfaces, where superposition of the Pentamer-NRP2 and Pentamer-THBD complexes demonstrates that these receptors share an overlapping binding site on Pentamer (Fig. 3C). Specifically, the common interaction site is localized at the interface where UL128 engages gL and is responsible for the binding of the NRP2 a1 domain and the THBD N-terminal lectin

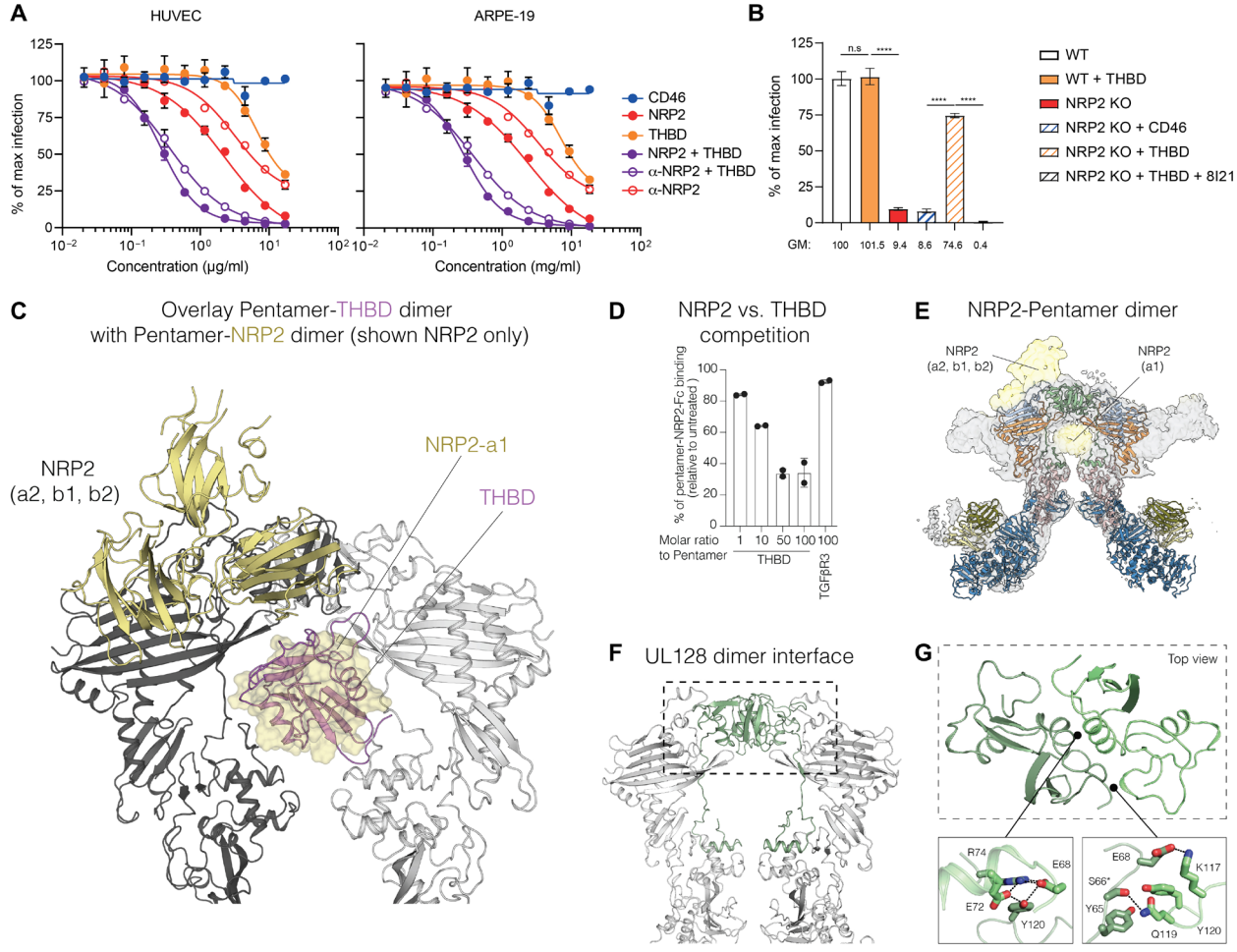

Fig. 3. THBD is a functional HCMV receptor and competes with NRP2 for HCMV Pentamer binding. (**A**) HUVEC or ARPE-19 cells were infected for 48 hours with VR1814 virus that had been preincubated with different concentrations of an anti-NRP2 antibody (red open circles), soluble recombinant CD46 (blue full circle), NRP2 (red full circle), THBD (orange full circle), a mix of recombinant NRP2 with THBD proteins (violet full circle), or a mix of anti-NRP2 with recombinant THBD proteins (violet full circle). The percentage of infected cells plotted against antibody or protein concentration is shown. The data shown are the means of three independent experiments ± SD. (**B**) Histogram representing the percentage of infection of HAP-1 cells WT or NRP2-KO that have been transduced with either empty lentivirus vector, lentivirus vector encoding CD46, or lentivirus vector encoding THBD. The percentage of maximum infection (geometric means of four independent experiments ± SD) is shown. n.s., not significant. (**C**) Overlay of HCMV Pentamer in complex with NRP2 and THBD. The a1 domain is shown in surface representation. (**D**) Binding of HCMV Pentamer to NRP2-Fc WT and increasing concentrations of THBD starting at equimolar ratio or addition of 100-fold excess of transforming growth factor β receptor 3 (TGFβR3) as a control. (**E**) Overlay between the HCMV Pentamer–NRP2 dimer cryo-EM map and the dimeric structure of HCMV Pentamer–THBD. (**F**) HCMV Pentamer dimerization interface mediated by UL128. (**G**) Close-in view of the dimeric interaction interface mediated by UL128 [top view relative to view in (G)].

domain, indicating that these interacting partners cannot bind the Pentamer at the same time (Fig. 3C). To test the observation, we performed competition experiments by incubating HCMV Pentamer bound to NRP2 with increasing amounts of THBD and observed that THBD can compete for NRP2 binding at high concentrations (Fig. 3D). Overall, our structural and biophysical data indicate that NRP2 and THBD do not function as co-receptors but rather mediate HCMV tropism by acting as independent receptors.

HCMV Pentamer dimers engage NRP2 and THBD in a similar architecture

The unexpected dimeric architecture of the Pentamer bound to NRP2 is highly similar to the dimeric population observed upon THBD binding (Fig. 3E). The a1 domain of NRP2 is encased between two Pentamer molecules analogous to the N-terminal lectin domain of THBD, whereas the a2b1b2 domains of NRP2 engage only one of the Pentamers to form a markedly asymmetric assembly (Fig. 3E). Notably, these two receptor super-assemblies also share a conserved dimerization interface mediated by a network of residues at the N-terminal region of the UL128 subunit localized at the most distal region of the Pentamer (Fig. 3, F and G), suggesting a potential physiological relevance of the dimeric assembly.

Structural basis for Pentamer neutralization by mAbs

Highly potent neutralizing antibodies against HCMV were isolated from immortalized memory B cells of HCMV-immune donors and have been shown to target conformational epitopes of the Pentamer (*8*, *18*). To provide a view of these neutralizing interactions, we determined the structure of Pentamer bound to the highly potent neutralizing Fabs 2C12 and 7I13, as well as bound to the gH binding Fab 13H11, to an overall resolution of ~2.9 Å (fig. S8). 2C12 binds the UL131A and UL128 subunits of the Pentamer in the same area recognized by NRP2 a2b1b2 domains (Fig. 4, A to E and J). Specifically, Y55, Y116, G119, and N120 from the light chain of 2C12 bind

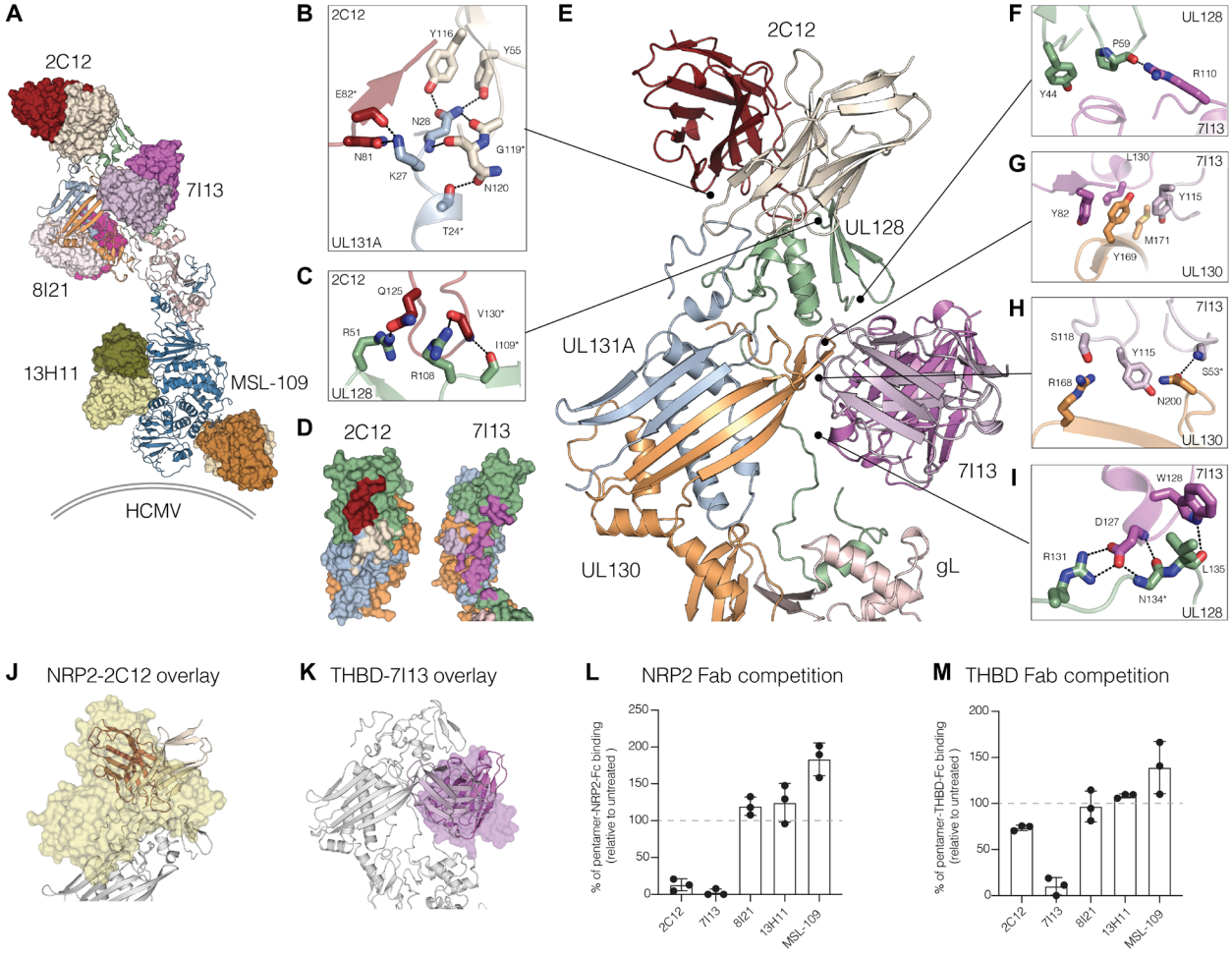

Fig. 4. Structural basis for HCMV Pentamer neutralization. (**A**) Front view of a composite structure of HCMV Pentamer complex (shown in ribbon) bound to the Pentamer-specific neutralizing antibodies 2C12, 7I13, and 8I21 (shown in surface representation) and the gH-specific neutralizing antibodies 13H11 and MSL-109 (shown in surface representation). (**B** and **C**) Close-in view of HCMV Pentamer distal region showing 2C12, UL128-131A, and gL with highlighted sites of interaction between Pentamer and 2C12. (**D**) Highlighted interaction interface between Pentamer and 2C12 or 7I13. (**E**) Close-in view of HCMV Pentamer distal region showing 2C12, UL128-131A, and gL 2C12 and 7I13. (**F** to **I**) Close-in view of HCMV Pentamer distal region showing 7I13, UL128-131A, and gL with highlighted sites of interaction between Pentamer and 7I13. (**J**) Overlay between HCMV Pentamer–NRP2 and HCMV Pentamer–2C12. (**K**) Overlay between HCMV Pentamer–THBD and HCMV Pentamer–7I13. (**L**) Binding of HCMV Pentamer to NRP2-Fc WT upon addition of the neutralizing Fabs 2C12, 7I13, 8I21, MSL-109, or 13H11. (**M**) Binding of HCMV Pentamer to THBD-Fc WT upon addition of the neutralizing Fabs 2C12, 7I13, 8I21, MSL-109, or 13H11.

the N-terminal region of UL131A between the residues T24-N28, while the heavy chain of 2C12 (N81, Q125, and V130) recognizes UL131A-K27 and UL128-R51, R108, and I109 (Fig. 4, B to E). Fab 7I13 buries a large footprint (~1200 Å^2) and binds to the same surface on the Pentamer that recognizes THBD and the NRP2 a1 domain (Fig. 4, E to I and K). Residues from both light and heavy chains of 7I13 contact UL128 on residues Y44, P59, R131, N134, and L135 and bind UL130 at R168, Y169, M171, and N200 through a combination of hydrophobic, polar, and charge interactions (Fig. 4, F to I). Fab 8I21, shown in the structure of the Pentamer-NRP2 complex (fig. S1), recognizes the Pentamer in a region nonoverlapping with THBD or NRP2 binding sites (Fig. 4A and fig. S9). Superposition of the 2C12-7I13-Pentamer and NRP2-Pentamer or THBD-Pentamer structures indicates that 2C12 blocks NRP2 but not THBD binding (Fig. 4J and fig. S9B), and a comparison of these structures suggests that 7I13 can block binding of both receptors, NRP2 and THBD (Fig. 4K and fig. S9C). Competition interaction experiments to Pentamer show that NRP2 binding is blocked by 2C12 and 7I13 but not by 8I21- or gH-specific neutralizing antibodies (Fig. 4L), whereas THBD binding is blocked by 7I13 but not by 2C12-, 8I21-, or gH-specific neutralizing antibodies (Fig. 4M).

DISCUSSION

We present a comprehensive structural, biophysical, and functional analysis of HCMV Pentamer to provide critical insight into its architecture, receptor recognition, cell entry, and neutralization. Our studies reveal how a large portion of the subunits UL128-131A of the Pentamer binds to two completely different functional receptor proteins, NRP2 and THBD, which sheds light on how HCMV achieves broad cellular tropism and receptor specificity of different cell types. NRP1 and NRP2 have been shown to use their b1 domain to interact with the CendR motif of binding partners including VEGF and spike protein of SARS-CoV-2 (*13*, *14*); however, structural studies, from our and McLellan's group, now demonstrate that NRP2 does not use this canonical binding site but instead engages the Pentamer through key interactions between the a2 and b2 domains to the UL128 and UL131A subunits (Fig. 1, E, F, and H, and fig. S3A) (*12*). Upon Pentamer binding, the NRP2 a1 domain is displaced from the a2b1b2 core and repositioned at the site of attachment between UL128 and gL (Fig. 1D). Intriguingly, the NRP2 a1 domain binds to the same region of Pentamer recognized by the THBD receptor (Figs. 1 and 2), indicating that HCMV Pentamer has evolved an opportunistic binding site able to recognize multiple distinct interacting partners with high affinity to enter different cell types.

Here, we show that THBD is a relevant functional receptor for HCMV (Fig. 3, A and B). The mutually exclusive binding of NRP2 and THBD to the Pentamer revealed by our structural and biophysical studies (Fig. 3, D to F) further suggests that HCMV likely uses the Pentamer to enter epithelial and endothelial cells through two alternative pathways rather than using these proteins as co-receptors. On the basis of NRP2 and THBD expression profile, it is tempting to speculate that the NRP2 receptor is principally used for epithelial

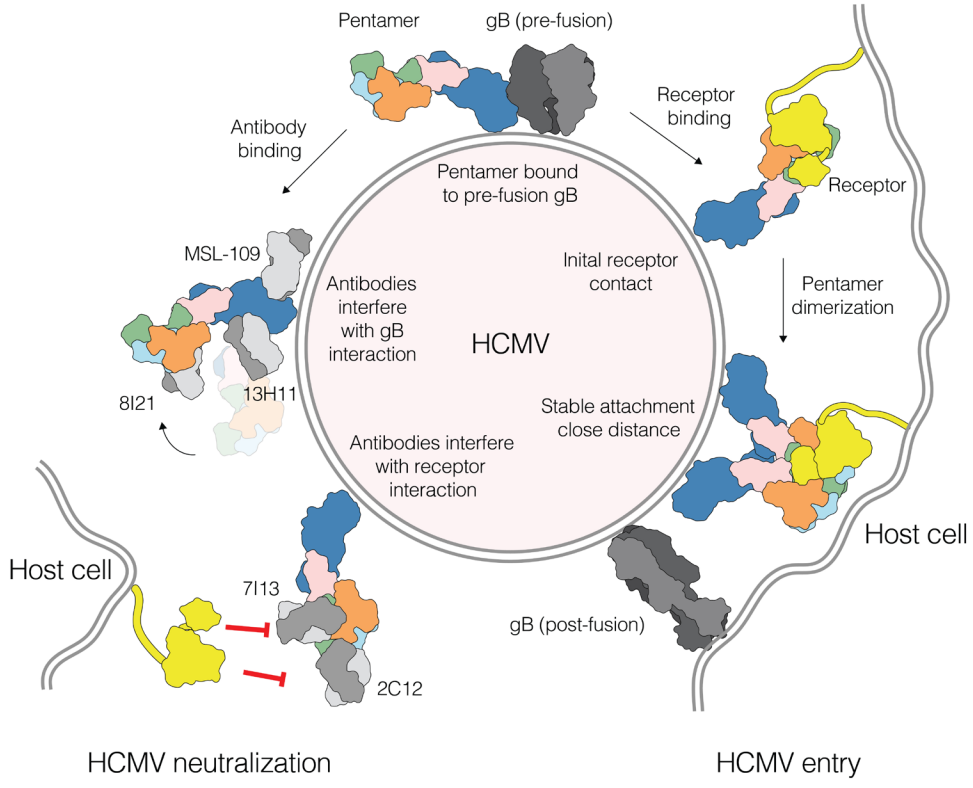

Fig. 5. Model for HCMV Pentamer neutralization and Pentamer-mediated cell entry. Receptor binding and possibly Pentamer dimerization could mediate receptor clustering and facilitate a high affinity and stable tethering of the viral membrane with the host cell membrane. Membrane tethering would trigger the transition of gB from its pre- to post-fusion conformation and initiate membrane fusion. A similar mechanism involving the Trimer, in the absence of receptor multimerization, has also been described (*16*).

cell infection, while THBD represents the main receptor for endothelial and myeloid cell infection (*19*, *20*). It was previously proposed that Pentamer would undergo a large conformational change upon receptor binding to trigger gB-mediated membrane fusion and HCMV entry (*15*). However, our structural studies suggest that NRP2 or THBD interactions do not substantially alter the conformation of the Pentamer (fig. S4, C and D). Hence, the Pentamer might trigger gB activation through a different mechanism without large Pentamer conformational changes, perhaps similar to what has been recently proposed for the HCMV Trimer (*16*).

Intriguingly, our structures reveal that HCMV Pentamer can undergo dimerization where the NRP2 a1 and THBD lectin–like domains become sandwiched in between two Pentamers. This apparent receptor-mediated dimerization of Pentamer occurs in a head-to-head fashion through the UL128 subunit and the NRP2 or THBD receptors (Figs. 2B and 3G). This mode of receptor engagement by Pentamer is distinctly different from what was observed for the HCMV Trimer, where each host receptor was seen to engage only one copy of the Trimer (*16*). It is notable that these structural observations appear consistent with the experimental designs required for the identification of the human receptors involved in Trimer or Pentamer recognition (*5*). While platelet-derived growth factor receptor α (PDGFRα) was identified as the Trimer receptor using a classic affinity purification approach (*21*), the identification of physiologically relevant Pentamer-receptor interactions could only be enabled through oligomerization of the Pentamer, likely via increased avidity for the receptors and potentially mimicking the molecular arrangement of two opposing membranes (i.e., the viral envelope and host cell) (*5*). While speculative, the apparent requirement for receptor-mediated dimerization of Pentamer and the lack of structural rearrangements upon receptor binding allow us to propose a potential mechanism for Pentamer-specific HCMV entry into host cells (Fig. 5). In this model, receptor binding is correlated with Pentamer dimerization and would, in turn, mediate receptor clustering to ultimately facilitate a high affinity and stable tethering of the viral membrane with the host cell membrane. Through a mechanism not yet known, receptor-mediated Pentamer dimerization and membrane tethering would trigger the transition of gB from its pre- to post-fusion conformation and initiate membrane fusion, perhaps through local trapping of gB and/or perturbations within the viral membrane bilayer upon Pentamer clustering. The recent high-resolution structure of HCMV gB in its prefusion conformation (*22*) should open new avenues to test these and other hypotheses. Future high-resolution structural studies will be required to address the structural basis of the HCMV Pentamer (or Trimer) interaction with prefusion gB and the mechanism required to trigger membrane fusion.

HCMV Pentamer elicits the most potent neutralizing antibody response against HCMV, but the structural basis for this neutralization has remained poorly understood. Our results show that Fab 2C12 directly interferes with NRP2 domain binding and blocks the attachment between Pentamer and NRP2 (Fig. 4). Fab 7I13 binds to a surface of the Pentamer that would block both NRP2 and THBD, representing a superior neutralizing antibody to block receptor interaction of the Pentamer and potentially Pentamer dimerization (Fig. 4). Overall, we present the structural basis for Pentamer receptor engagement and neutralization, which reveals insights into the broad cellular tropism and cell entry mechanism of HCMV. We anticipate that our findings will provide a framework for the future development of effective vaccines and therapeutics against HCMV.

MATERIALS AND METHODS

Generation of HCMV glycoprotein and Fab constructs

Codon-optimized (for expression in human cells) HCMV gH, gL, UL128, UL130, UL131A, and NRP2 genes were synthesized and subcloned into the plasmid expression vector pRK5 (Genentech). The gH gene comprised only the extracellular region (first 716 amino acids) and was fused to a C-terminal Myc-Avi-8×HIS tag. For protein purification purposes, UL130 was fused to a C-terminal double Strep-tag.

Protein expression and purification

HCMV Pentamer was purified in three steps as previously described for HCMV Trimer (*16*). Expi293F cells were transfected with plasmids encoding individual subunits. The expression supernatant corresponding to a 50-liter expression was concentrated via tangential flow filtration (TFF) to a volume of 1 to 2 liters, loaded on a 20-ml Ni Sepharose Excel (Cytiva) resin, washed with 13 column volumes (CVs) of wash buffer [50 mM tris (pH 8.0), 300 mM NaCl, 5% glycerol, and 20 mM imidazole], and eluted in 5 CVs of elution buffer [50 mM tris (pH 8.0), 300 mM NaCl, 5% glycerol, and 400 mM imidazole]. The eluent was applied to 3 ml of Strep-Tactin XT high affinity resin (IBA) and bound for 2 hours. The resin was washed with 10 CVs of Strep-wash buffer [25 mM Hepes (pH 7.5), 300 mM NaCl, and 5% glycerol] and eluted from the beads in Strep-wash buffer supplemented with 50 mM biotin. The eluate was concentrated with an Amicon Ultra centrifugal filter device [30 kDa molecular weight cutoff (MWCO)] and loaded on a Superdex 200 10/300 or 16/60 column equilibrated in Pentamer–size exclusion chromatography (SEC) buffer [25 mM Hepes (pH 7.5), 300 mM NaCl, and 5% glycerol].

Human Fc–tagged NRP2 proteins were expressed in 30-ml cultures of Expi293F cells, transfected with 30 μg of plasmid DNA, and grown for 7 days. After harvesting the expression medium culture supernatants, the Fc-fusion proteins were purified with 0.15 ml of Toyopearl AF-r Protein A HC-650F (Tosoh Bioscience, Grove City, OH). Unbound proteins and medium components were removed by washing with 10 CVs of phosphate-buffered saline (PBS; pH 7.4). NRP2-huFc fusions were eluted from the resin using elution buffer [50 mM phosphoric acid (pH 2.9)] and immediately neutralized to a pH of ~6.0 by adding 0.05 ml of 20× PBS (pH 11.0). The proteins were further polished by SEC purification, performed on a Zenix-C SEC 300 column (Sepax Technology, Newark, DE), and connected to an UltiMate 3000 high-performance liquid chromatography system (Thermo Fisher Scientific, Waltham, MA). The column was equilibrated in 1× PBS (pH 7.4), and the samples were separated by isocratic elution at a flow rate of 1.5 ml/min.

Human THBD-Flag and NRP2-Flag were purified from a 10-liter expression supernatant. The supernatant was incubated with 10 ml of M2 agarose Flag resin (Sigma-Aldrich) and incubated for 20 hours at 4°C. The resin was washed with 10 CVs of FLAG-wash buffer [25 mM Hepes (pH 7.5), 200 mM NaCl, and 5% glycerol] and eluted with FLAG-wash buffer supplemented with FLAG peptide (0.2 mg/ml). The eluate was concentrated with an Amicon Ultra centrifugal filter device (30 kDa MWCO) and loaded on a Superdex 200 10/60 column equilibrated in SEC buffer [25 mM Hepes (pH 7.5), 200 mM NaCl].

The heavy and light chains of Fab MSL-109 were coexpressed under a phoA promoter in *Escherichia coli* 34B8 cells (in-house strain) in phosphate-limiting medium (C.R.A.P.) for 20 hours at 30°C. The pellet from a 1-liter expression was resuspended in 70 ml

of lysis buffer (1× PBS and 25 mM EDTA) supplemented with Roche protease inhibitor tablets and lysed by sonication. The lysate was cleared by centrifugation at 25,000*g* for 1 hour and subsequently passed through a 0.45-μm filter. The cleared lysate was loaded onto a 5-ml HiTrap Protein G HP (Cytiva) column that was equilibrated in lysis buffer. The column was washed with 10 to 20 CVs of lysis buffer and eluted in 0.58% (v/v) acetic acid. The pH of the eluate was immediately adjusted by addition of SP-A buffer [20 mM MES (pH 5.5)] and loaded onto a 5-ml HiTrap SP HP cation exchange chromatography column (Cytiva). The Fab was eluted in a linear 20-CV gradient to SP-B buffer [20 mM MES (pH 5.5) and 500 mM NaCl]. The eluate was concentrated using an Amicon Ultra centrifugal filter device (10 kDa MWCO) and further purified on a Superdex 200 10/300 column equilibrated in Fab-S200 buffer [25 mM tris (pH 7.5) and 300 mM NaCl]. The purified Fab was concentrated with an Amicon Ultra centrifugal filter device (10 kDa MWCO), frozen in liquid N_2, and stored at −80°C. The heavy and light chains of Fab 2C12, 7I13, 8I21, or 13H11 were coexpressed under a phoA promoter in *E. coli* 34B8 cells (in-house strain) in phosphate-limiting medium (C.R.A.P.) for 20 hours at 30°C. The pellet from a 4-liter expression was resuspended in 250 ml of lysis buffer [25 mM tris (pH7.5), 150 mM NaCl, 5 mM EDTA, and 2 mM NaN_3] supplemented with Roche protease inhibitor tablets and lysed by sonication. Subsequent purification followed similar protocol as described for MSL-109.

Complexes between the Pentamer, Fabs, and THBD were generated by incubation for at least 1 hour on ice with at least 1.2 molar excess of Fab and receptors and purified by SEC to remove excess Fab/receptors. Pentamer-NRP2-Fab complexes were formed in two steps. First, Pentamer and NRP2 were mixed and purified by SEC followed by addition of excess of Fabs 8I21 and 13H11 and a second SEC purification.

Cryo-EM sample preparation and data acquisition

The HCMV Pentamer complexes shown in this study were prepared as previously described for HCMV Trimer (*16*). For the HCMV Pentamer gHgL-UL128-UL130-UL131A + NRP2 + 8I21 + 13H11 complex, holey carbon grids (Ultrafoil 25 nM Au R 0.6/1 300 mesh; Quantifoil) were glow-discharged for 20 s using a Solarus plasma cleaner (Gatan). For all other Pentamer complexes, holey carbon grids (Ultrafoil 25 nM Au R 0.6/1 300 mesh; Quantifoil) were incubated with a thiol-reactive, self-assembling reaction mixture of 4 mM monothiolalkane(C11)PEG6-OH (11-mercaptoundecyl) hexaethyleneglycol (SPT-0011P6, SensoPath Technologies Inc., Bozeman, MT) (*23*). Grids were incubated with this self-assembled monolayer (SAM) solution for 24 hours. Before grid freezing, grids were removed from the SAM solution and rinsed with EtOH. The sample (3 μl) at a concentration of 0.66 to 1.8 mg/ml was applied to the grid and blotted single-sided with a Leica EM GP (Leica) using 3.5-s blotting time with 100% humidity and plunge-frozen in liquid ethane cooled by liquid nitrogen. The Pentamer-NRP2-8I21-13H11 sample was mildly cross-linked with 0.025% EM-grade glutaraldehyde for 10 min at room temperature and quenched with 9 mM tris (pH 7.5) before grid application.

Movie stacks for HCMV Pentamer gHgL-UL128-UL130-UL131A + 2C12 + 7I13 + 13H11 and HCMV Pentamer gHgL-UL128-UL130-UL131A + NRP2 + 8I21 + 13H11 were collected using SerialEM (*24*) on a Titan Krios operated at 300 keV with bioquantum energy filter equipped with a K2 Summit direct electron detector camera (Gatan). Images were recorded at a magnification of ×165,000 corresponding to 0.824 Å per pixel, using a 20-eV energy slit. Each image stack contains 50 frames recorded every 0.2 s for an accumulated dose of ~50 e $Å^{-2}$ and a total exposure time of 10 s. Images were recorded with a set defocus range of 0.5 to 1.5 μm.

Movie stacks for HCMV Pentamer gHgL-UL128-UL130-UL131A + THBD + MSL-109 + 13H11 were collected using SerialEM (*24*) on Titan Krios G3i (Thermo Fisher Scientific, Waltham, MA) operated at 300 keV with bioquantum energy filter equipped with a K3 Summit direct electron detector camera (Gatan Inc., Pleasanton, CA). Images were recorded in EFTEM mode at a magnification of ×105,000 corresponding to 0.838 Å per pixel, using a 20-eV energy slit. Each image stack contains 60 frames recorded every 0.05 s for an accumulated dose of ~60 e $Å^{-2}$ and a total exposure time of 3 s. Images were recorded with a set defocus range of 0.5 to 1.5 μm.

Cryo-EM data processing

Cryo-EM data were processed using a combination of the RELION (*25*), cisTEM (*26*), and cryoSparc (*27*) software packages, similarly to our previous work on HCMV Trimer (*16*). The HCMV Pentamer–2C12–7I13–13H11 cryo-EM data were processed as described in fig. S8. For the generation of the first ab initio reconstruction, 18,326 movies were motion-corrected and contrast-transfer function parameters were fit within cisTEM. A total of 1,527,802 potential particles were picked using the circular blob picking tool within cisTEM. Particles were sorted in two rounds of cisTEM 2D classification to select the best aligning particles yielding 184,833 particles. These particles were subjected to an ab initio 3D generation within cisTEM with three target volumes. The volume corresponding to HCMV Pentamer bound to Fabs 2C12, 7I13, and 13H11 was used as a 3D reference for the high-resolution 3D refinements. For the generation of a high-resolution 3D reconstruction of the Pentamer-2C12-7I13-13H11 complex, all 18,326 movies were corrected for frame motion using the MotionCor2 (*28*) implementation in RELION and contrast-transfer function parameters were fit using the 30- to 4.5-Å band of the spectrum with CTFFIND-4 (*29*). Contrast transfer function (CTF) fitted images were filtered on the basis of the detected fit resolution better than 8 Å. A total of 5,128,264 particles were picked by template matching with gautomatch (www2.mrc-lmb.cam.ac.uk/research/locally-developed-software/zhang-software/#gauto) using a 30-Å low-pass–filtered Pentamer-2C12-7I13-13H11 complex reference structure. Particles were sorted during RELION 2D classification, and 4,792,984 selected particles were imported into cisTEM for 3D refinements. The first Pentamer-2C12-7I13-13H11 reconstruction was obtained after auto-refine and manual refinements with a mask around the Pentamer-2C12-7I13-13H11 complex and by applying low-pass filter outside the mask (filter resolution, 20 Å) and a score threshold of 0.30 so that only the best-scoring 30% of particle images would be included in the 3D reconstruction at each cycle. The weight outside of the mask was incrementally reduced from 0.5 to 0.15 in iterative rounds of manual refinements (no data beyond 3.8 Å were used in the refinement). To improve the quality of the map, focused refinements were conducted after dividing the map into three distinct regions using masks and applying low-pass filter outside the mask (filter resolution, 20 Å) and a score threshold of 0.20. The focused maps were sharpened in cisTEM with the following parameters: flattening from a resolution of 8 Å, applying a pre-cutoff *B*-factor of −90 $Å^2$ from the origin of reciprocal space to 8 Å, and applying a

figure-of-merit filter (*30*). For model building and figure preparation, a composite map was generated from the three individual focused 3D maps using phenix combine_focused_maps (*31*).

The HCMV Pentamer–THBD–13H11–MSL-109 cryo-EM data were processed as described in fig. S5. The 10,926 movies were motion-corrected using Relion's implementation of motion correction, and the aligned micrographs were imported into cisTEM for CTF estimation via CTFFIND4. A total of 9167 images with CTF fit resolutions of at least 5 Å were selected for ab initio particle picking using an exclusion and template radius of 30 Å. The resulting 10,680,163 particle coordinates were extracted using a 400-pixel box size and 1.07 Å per pixel. Multiple rounds of hierarchical 2D classification and class selection ultimately resulted in three particle stacks: a 78,577-particle stack consisting of 2D classes in which an entire dimer was clearly resolved, a 172,398-particle stack containing several additional classes in which the dimer was nearly fully resolved, and a 504,492-particle stack containing all 2D classes with at least some well-resolved regions. An ab initio C2 symmetric 3D map was generated from the 78,577-particle stack, and automatic 3D refinement using C2 symmetry resulted in an initial intermediate-resolution initial map. The 172,398-particle stack was exported to Relion, and the C2 symmetric initial map was used as a template for 3D auto-refinement, first in C2 and ultimately using C1 symmetry with C2 symmetry relaxation. This resulted in an intermediate-resolution HCMV Pentamer dimer map in which a single asymmetrically bound THBD was resolved at the dimer interface. Returning to cisTEM, the most inclusive 504,492-particle stack was then refined in C1 against this asymmetric map, using a full-molecule mask and also three different focused masks: one that included only THBD and UL128, UL130, and UL131 of both protomers, one that included only gL, gH, 13H11, and MSL-109 of a single protomer of the pseudodimer, and one that included only gL, gH, 13H11, and MSL-109 of the other protomer. Phenix ResolveCryoEM density modification was applied to each of these, and the final map used for model building was generated by combining the density-modified maps in UCSF Chimera by fitting the focused maps to the full-molecule map by correlation, resampling to a common grid, and taking the highest value between the three focused maps for each voxel (vop maximum). Local resolution was calculated from the unsharpened, unfiltered half maps using Relion postprocessing.

The HCMV Pentamer–NRP2–13H11–8I21 cryo-EM data were processed as described in fig. S1. The 21,357 movies were motion-corrected using Relion, CTF parameters were estimated with CTFFIND4, and images with CTF fit resolutions of at least 5 Å were selected for further processing. Relion ab initio Laplace-of-Gaussian particle picking resulted in 982,313 particle coordinates, which were extracted using a box size of 142 pixels and a pixel size of 3 Å. After 2D classification, 2D classes of apparent HCMV pentamers (69,767 particles) were reextracted to a box size of 400 pixels and 1.07 Å per pixel and subjected to Relion ab initio 3D refinement followed by 3D auto-refinement, resulting in an initial pentamer map. For the dimeric Pentamer-NRP2-8I21-13H11, 2D class selections were used as templates for Relion template–based particle picking, resulting in 1,300,844 coordinates. These coordinates were extracted to a box size of 400 pixels and 1.07 Å per pixel and subjected to hierarchical 2D classification and selection, ultimately resulting in 72,745 particles. These particles were imported directly to cisTEM and refined against the initial dimeric pentamer map using a full-molecule mask (no data beyond 6.7 Å were used in the refinement). For the monomeric Pentamer-NRP2-8I21-13H11 complexes, 21,357 images with CTF fit resolutions of at least 6 Å were selected for further processing. A total of 2,532,206 particles were picked by template matching with projections from 30-Å low-pass–filtered single Pentamer-NRP2-8I21-13H11 reconstructions with gautomatch (www2.mrc-lmb.cam.ac.uk/research/locally-developed-software/zhang-software/#gauto). Particles were extracted using a box size of 66 pixels and a pixel size of 5.4 Å and sorted using Relion 2D classification, and 2,252,924 particles were extracted with a box size of 280 pixels and a pixel size of 1.35 Å. These particles were imported directly to cisTEM and refined against the initial monomeric pentamer map using a full-molecule mask (no data beyond 4 Å were used in the refinement). To improve the quality of the map, focused refinements were conducted after dividing the map into three distinct regions using masks and applying low-pass filter outside the mask (filter resolution, 20 Å) and a score threshold of 0.20. Phenix ResolveCryoEM density modification was applied to each of these maps, and the final map used for model building was then generated by combining the density-modified maps in UCSF Chimera. Local resolution was calculated from the unsharpened, unfiltered half maps using Relion postprocessing for the dimeric Pentamer-NRP2-8I21-13H11. For the monomeric Pentamer-NRP2-8I21-13H11 complex, local resolution was determined in cisTEM using a re-implementation of the blocres algorithm.

Model building and structure analysis

The gH, gL, UL128, UL130, and UL131A subunits of the HCMV Pentamer structure (*15*) were fit as a rigid body into the cryo-EM map. The THBD lectin domain was built on the basis of a homology model of human RegIIalpha [PDB: 4MTH; (*32*)] using SwissModel (*33*). The structure of NRP2 (PDB: 2QQO) was used as a template for modeling of NRP2 a1-a2-b1b2 domains. The resulting model was fit as a rigid body into the cryo-EM map. After extensive rebuilding and manual adjustments, multiple rounds of real-space refinement using the phenix.real_space_refinement (*31*) tool were used to correct global structural differences between the initial model and the map. The model was further manually adjusted in Coot (*34*) through iterative rounds of model building and real-space refinements in Isolde (*35*) and Phenix (*31*). The model was validated using phenix.validation_cryoem (*31*) with built-in MolProbity scoring (*36*). Figures were made using PyMOL (The PyMOL Molecular Graphics System v.2.07, Schrödinger LLC) and UCSF ChimeraX (*37*). Sequences were aligned using Clustal Omega (*38*) within JalView (*39*) and illustrated with ESPript 3.0 (*40*).

Cells and viruses

Cells used for these studies were the same as in our previous work carried out to identify HCMV receptors (*5*). ARPE-19 is a male cell line derived from the spontaneously arising retinal pigment epithelia cell line [American Type Culture Collection (ATCC) CRL-2302] and was cultured in Dulbecco's modified Eagle's medium (DMEM)/F-12 + GlutaMAX (Thermo Fisher Scientific) supplemented with 10% fetal bovine serum (FBS) and penicillin-streptomycin (Thermo Fisher Scientific). HAP-1 cell is a male chronic myelogenous leukemia cell line derived from KBM-7 cell line obtained from Horizon Genomics GmbH and cultured in Iscove's modified Dulbecco's medium + GlutaMAX in the presence of 10% FBS and penicillin-streptomycin. Human umbilical vein endothelial cells (HUVECs; pooled from male and female donors) obtained from Lonza and provided

by Fondazione IRCCS Policlinico San Matteo (Pavia, Italy) were cultured in EndoGRO-VEGF Complete Media (Millipore). Human embryonic kidney (HEK) 293FT is a female HEK cell line isolate derived from HEK cells transformed with the SV40 large T antigen (Thermo Fisher Scientific). The 293FT cell line was cultured in DMEM + 10% FBS, 0.1 mM minimum essential medium (MEM) nonessential amino acids, GlutaMAX, 1 mM MEM sodium pyruvate, and geneticin (500 mg/ml; Thermo Fisher Scientific). All cell lines were confirmed to be free of mycoplasma. HCMV clinical isolate VR1814 was provided by Virologia e Microbiologia, Fondazione IRCCS Policlinico San Matteo (Pavia, Italy). HCMV VR1814 was propagated in HUVECs. ARPE-19, HUVEC, and HAP-1 cells are not listed according to International Cell Line Authentication Committee (ICLAC) 3/10/2014. ARPE-19 and HAP-1 cells were authenticated by analysis of short tandem repeat loci at ATCC and Horizon Genomics GmbH, respectively. HUVECs were authenticated by expression of CD31/105 and von Willebrand factor VIII and are positive for acetylated low-density lipoprotein uptake. HEK293FT cells were purchased from Thermo Fisher Scientific and authenticated by their ability to produce high-titer infective lentiviral particles.

Flow cytometry staining

Flow cytometry staining procedures were the same as in our previous work carried out to identify HCMV receptors (*5*). For cell surface staining, adherent cells (ARPE-19, HUVEC, and HAP-1) were gently detached with a cell scraper, washed twice with PBS + 2% FBS, and incubated in PBS + 0.5% bovine serum albumin (BSA) + 2 mM EDTA with specific anti-NRP2 and anti-CD46 antibodies (AF2215 and AF2005, R&D Systems), anti-THBD antibody (clone 141C01, Abcam), or, as isotype control, normal sheep immunoglobulin G (IgG) affinity pure (R&D Systems) at 2 μg/ml for 30 min on ice. After two washes, cells were incubated with anti-mouse IgG (H+L) Alexa Fluor 594–conjugated (Thermo Fisher Scientific) secondary antibodies at 2 mg/ml for 30 min on ice, washed twice, and acquired with a FACS (fluorescence-activated cell sorting) Fortessa (BD Biosciences) flow cytometer. Analysis was performed with FlowJo software (TreeStar).

Virus microneutralization

Serial dilutions of antibodies and soluble recombinant proteins were preincubated with HCMV clinical isolate (strain VR1814) for 1 hour at 37°C and added to confluent monolayers of ARPE-19, HUVEC, or HAP-1 cells cultured in 96-well flat-bottom plates [multiplicity of infection (MOI) of 1]. Serial dilution (1:3) was used for microneutralization assay, with the first dilution at 20 μg/ml. Infected cells were harvested after 3 days, fixed with BD Cytofix/Cytoperm (Thermo Fisher Scientific), washed twice with PBS + 2% FBS, and incubated in PBS + 0.5% BSA + 2 mM EDTA with specific mouse anti-pp72 antibody (clone 6E1, SC-69834, Santa Cruz Biotechnology) or isotype control at 2 μg/ml for 30 min on ice. After two washes, cells were incubated with goat anti-mouse IgG (H+L) Alexa Fluor 647–conjugated (Thermo Fisher Scientific) secondary antibodies at 2 μg/ml for 30 min on ice. Samples were acquired with a FACS Fortessa (BD Biosciences) flow cytometer. Analysis was performed with FlowJo software (TreeStar). The percentage of infected cells was calculated by FACS. Dose-response curves were generated by plotting the relative infected cells against mean fluorescence intensity (MFI) signal. The concentration causing inhibition of 50% of infection (IC_{50}) was calculated by nonlinear regression with Prism 8 (GraphPad Software).

Gene overexpression and gene KO

Gene overexpression and KO for these studies were the same as in our previous work carried out to identify HCMV receptors (*5*). Human Nrp2 (accession no. AF022860), CD46 (accession no. NM_002389), and THBD (accession no. AF495471) were ordered from GenEZ ORF database (GenScript) and cloned in pCDH-EF1-MCS (System Biosciences). Lentiviral particles were generated by polyethylenimine transfection of 293FT (Thermo Fisher Scientific) with pCDH-EF1-MCS (System Biosciences), pMD2.G (Addgene), and psPAX (Addgene) and purified on a sucrose cushion. HAP-1 KO by CRISPR-Cas9 of NRP2 was generated by Horizon Genomics GmbH. HAP-1 cells transduced with lentivirus were selected for 3 days with puromycin (0.5 mg/ml; Thermo Fisher Scientific). Single clones were expanded, and effective KO of the target gene was analyzed by flow cytometry and confirmed by Sanger sequencing. Sequence of the guide RNAs used for CRISPR-Cas9 of Nrp2 is listed thereafter. Nrp2: 5′_GGGTAGTCCTGGGGGTAACC_3′.

Spreading assay

To investigate cell spreading, HAP-1 cell monolayers were inoculated with HCMV VR1814 at an MOI of 0.1 plaque-forming unit per cell (virus was titrated on ARPE-19 cells). Infected cell cultures were then stained at day 2 or 8 with mouse anti-pp72 antibody (clone 6E1, SC-69834, Santa Cruz Biotechnology) or isotype control at 2 μg/ml for 30 min on ice. Infected HAP1-Nrp2 KO were used as control and did not show the presence of any infection.

Biolayer interferometry

The interactions between NRP2, THBD, Fabs proteins, and HCMV Pentamer were analyzed by biolayer interferometry using an Octet Red96 system (ForteBio) as previously described (*16*). All data were collected at 25°C using 96-well black flat-bottom plates (Greiner Bio-One). Recombinant NRP2-Fc or THBD-Fc proteins were captured onto anti-human Fc–coated (AHC) sensors (Sartorius) and tested for binding to the CMV Pentamer as soluble analyte. Sensors were equilibrated for 10 min before the assay in PBS following the manufacturer's instructions. All steps—loading, baseline, association, and dissociation—were performed in PBS.

For comparison of relative binding between HCMV Pentamer and the NRP2 WT and mutant proteins, the NRP2-Fc proteins were captured onto AHC sensors and tested for binding to the Pentamer as soluble analyte at 50 nM concentration. Binding to NRP2 mutant proteins was represented relative to binding to the NRP2 WT protein. Binding units at the end of the association step were used to calculate the relative binding shown in the plot. For the NRP2-THBD competition experiment, THBD-Flag was added at different concentrations (1:1, 1:10, 1:50, and 1:100 molar excess) relative to the preequilibrated Pentamer-NRP2-Fc complex. For the Fab competition experiment, Fabs 2C12, 7I13, 8I21, 13H11, or MSL-109 were added in excess at a concentration of 100 μg/ml to the preequilibrated Pentamer-NRP2-Fc complex. In all cases, data were acquired using the Octet Red instrument (Forte Pall software version 9.0), and subsequently, the BIAevaluation software version 4.1 (GE Healthcare) was used for calculations of kinetic parameters. Data were fit to a 1:1 Langmuir binding model.

Quantification and statistical analysis

In figs. S1, S4, and S6, the resolution estimations of cryo-EM density maps are based on the 0.143 Fourier shell correlation criterion (*30*).

In Fig. 3 (A and B) statistical parameters including the exact value of n, precision measures (geometric mean ± SEM) and statistical significance are reported in the figures and figure legends. Data were judged to be statistically significant when $P < 0.05$. No statistical methods were used to predetermine sample size, no blinding of investigators was required, and no data points were excluded. Data were analyzed with Prism 8 (GraphPad Software) using the two-tailed nonparametric Mann-Whitney U test for two groups' comparison, or Kruskal-Wallis test (and Dunn's posttest) when three or more groups were compared (asterisks denote statistical significance: $*P < 0.05$; $**P < 0.01$; $***P < 0.001$; $****P < 0.0001$). Cell surface interaction screen data were analyzed and represented using Microsoft Excel (version 14.7).

SUPPLEMENTARY MATERIALS

Supplementary material for this article is available at https://science.org/doi/10.1126/sciadv.abm2536

REFERENCES AND NOTES

1. C. N. Kotton, Management of cytomegalovirus infection in solid organ transplantation. *Nat. Rev. Nephrol.* **6**, 711–721 (2010).
2. T. B. Hyde, D. S. Schmid, M. J. Cannon, Cytomegalovirus seroconversion rates and risk factors: Implications for congenital CMV. *Rev. Med. Virol.* **20**, 311–326 (2010).
3. S. A. Connolly, T. S. Jardetzky, R. Longnecker, The structural basis of herpesvirus entry. *Nat. Rev. Microbiol.* **19**, 110–121 (2021).
4. X. E, P. Meraner, P. Lu, J. M. Perreira, A. M. Aker, W. M. McDougall, R. Zhuge, G. C. Chan, R. M. Gerstein, P. Caposio, A. D. Yurochko, A. L. Brass, T. F. Kowalik, OR14I1 is a receptor for the human cytomegalovirus pentameric complex and defines viral epithelial cell tropism. *Proc. Natl. Acad. Sci. U.S.A.* **116**, 7043–7052 (2019).
5. N. Martinez-Martin, J. Marcandalli, C. S. Huang, C. P. Arthur, M. Perotti, M. Foglierini, H. Ho, A. M. Dosey, S. Shriver, J. Payandeh, A. Leitner, A. Lanzavecchia, L. Perez, C. Ciferri, An unbiased screen for human cytomegalovirus identifies neuropilin-2 as a central viral receptor. *Cell* **174**, 1158–1171.e19 (2018).
6. C. C. Nguyen, J. P. Kamil, Pathogen at the gates: Human cytomegalovirus entry and cell tropism. *Viruses* **10**, 704 (2018).
7. E. Malito, S. Chandramouli, A. Carfi, From recognition to execution—The HCMV Pentamer from receptor binding to fusion triggering. *Curr. Opin. Virol.* **31**, 43–51 (2018).
8. A. Macagno, N. L. Bernasconi, F. Vanzetta, E. Dander, A. Sarasini, M. G. Revello, G. Gerna, F. Sallusto, A. Lanzavecchia, Isolation of human monoclonal antibodies that potently neutralize human cytomegalovirus infection by targeting different epitopes on the gH / gL / UL128-131A complex. *J. Virol.* **84**, 1005–1013 (2010).
9. K. K. Biron, Antiviral drugs for cytomegalovirus diseases. *Antiviral Res.* **71**, 154–163 (2006).
10. S.-J. Chen, S.-C. Wang, Y.-C. Chen, Antiviral agents as therapeutic strategies against cytomegalovirus infections. *Viruses* **12**, 21 (2019).
11. C. Ciferri, S. Chandramouli, D. Donnarumma, P. A. Nikitin, M. A. Cianfrocco, R. Gerrein, A. L. Feire, S. W. Barnett, A. E. Lilja, R. Rappuoli, N. Norais, E. C. Settembre, A. Carfi, Structural and biochemical studies of HCMV gH/gL/gO and Pentamer reveal mutually exclusive cell entry complexes. *Proc. Natl. Acad. Sci. U.S.A.* **112**, 1767–1772 (2015).
12. D. Wrapp, X. Ye, Z. Ku, H. Su, H. G. Jones, N. Wang, A. K. Mishra, D. C. Freed, F. Li, A. Tang, L. Li, D. K. Jaijyan, H. Zhu, D. Wang, T.-M. Fu, N. Zhang, Z. An, J. S. McLellan, Structural basis for HCMV Pentamer recognition by antibodies and neuropilin 2. bioRxiv 2021.03.25.436804 [Preprint]. 25 March 2021. https://doi.org/10.1101/2021.03.25.436804.
13. J. L. Daly, B. Simonetti, K. Klein, K. E. Chen, M. K. Williamson, C. Antón-Plágaro, D. K. Shoemark, L. Simón-Gracia, M. Bauer, R. Hollandi, U. F. Greber, P. Horvath, R. B. Sessions, A. Helenius, J. A. Hiscox, T. Teesalu, D. A. Matthews, A. D. Davidson, B. M. Collins, P. J. Cullen, Y. Yamauchi, Neuropilin-1 is a host factor for SARS-CoV-2 infection. *Science* **370**, 861–865 (2020).
14. M. W. Parker, P. Xu, X. Li, C. W. Vander Kooi, Structural basis for selective vascular endothelial growth factor-A (VEGF-A) binding to neuropilin-1. *J. Biol. Chem.* **287**, 11082–11089 (2012).
15. S. Chandramouli, E. Malito, T. Nguyen, K. Luisi, D. Donnarumma, Y. Xing, N. Norais, D. Yu, A. Carfi, Structural basis for potent antibody-mediated neutralization of human cytomegalovirus. *Sci. Immunol.* **2**, eaan1457 (2017).
16. M. Kschonsak, L. Rougé, C. P. Arthur, H. Hoangdung, N. Patel, I. Kim, N. C. Johnson, E. Kraft, A. L. Rohou, A. Gill, N. Martinez-Martin, J. Payandeh, C. Ciferri, Structures of HCMV Trimer reveal the basis for receptor recognition and cell entry. *Cell* **184**, 1232–1244.e16 (2021).
17. B. A. Appleton, P. Wu, J. Maloney, J. P. Yin, W. C. Liang, S. Stawicki, K. Mortara, K. K. Bowman, J. M. Elliott, W. Desmarais, J. F. Bazan, A. Bagri, M. Tessier-Lavigne, A. W. Koch, Y. Wu, R. J. Watts, C. Wiesmann, Structural studies of neuropilin/antibody complexes provide insights into semaphorin and VEGF binding. *EMBO J.* **26**, 4902–4912 (2007).
18. C. Ciferri, S. Chandramouli, A. Leitner, D. Donnarumma, M. A. Cianfrocco, R. Gerrein, K. Friedrich, Y. Aggarwal, G. Palladino, R. Aebersold, N. Norais, E. C. Settembre, A. Carfi, Antigenic characterization of the HCMV gH/gL/gO and pentamer cell entry complexes reveals binding sites for potently neutralizing human antibodies. *PLOS Pathog.* **11**, e1005230 (2015).
19. S. E. Sartain, N. A. Turner, J. L. Moake, TNF regulates essential alternative complement pathway components and impairs activation of protein c in human glomerular endothelial cells. *J. Immunol.* **196**, 832–845 (2016).
20. A. Bachem, S. Güttler, E. Hartung, F. Ebstein, M. Schaefer, A. Tannert, A. Salama, K. Movassaghi, C. Opitz, H. W. Mages, V. Henn, P. M. Kloetzel, S. Gurka, R. A. Kroczek, Superior antigen cross-presentation and XCR1 expression define human $CD11c^{+}CD141^{+}$ cells as homologues of mouse CD8+ dendritic cells. *J. Exp. Med.* **207**, 1273–1281 (2010).
21. A. Kabanova, J. Marcandalli, T. Zhou, S. Bianchi, U. Baxa, Y. Tsybovsky, D. Lilleri, C. Silacci-Fregni, M. Foglierini, B. M. Fernandez-Rodriguez, A. Druz, B. Zhang, R. Geiger, M. Pagani, F. Sallusto, P. D. Kwong, D. Corti, A. Lanzavecchia, L. Perez, Platelet-derived growth factor-α receptor is the cellular receptor for human cytomegalovirus gHgLgO trimer. *Nat. Microbiol.* **1**, 16082 (2016).
22. Y. Liu, K. P. Heim, Y. Che, X. Chi, X. Qiu, S. Han, P. R. Dormitzer, X. Yang, Prefusion structure of human cytomegalovirus glycoprotein B and structural basis for membrane fusion. *Sci. Adv.* **7**, eabf3178 (2021).
23. J. R. Meyerson, P. Rao, J. Kumar, S. Chittori, S. Banerjee, J. Pierson, M. L. Mayer, S. Subramaniam, Self-assembled monolayers improve protein distribution on holey carbon cryo-EM supports. *Sci. Rep.* **4**, 7084 (2014).
24. D. N. Mastronarde, Automated electron microscope tomography using robust prediction of specimen movements. *J. Struct. Biol.* **152**, 36–51 (2005).
25. S. H. W. Scheres, RELION: Implementation of a Bayesian approach to cryo-EM structure determination. *J. Struct. Biol.* **180**, 519–530 (2012).
26. T. Grant, A. Rohou, N. Grigorieff, *cis*TEM, user-friendly software for single-particle image processing. *eLife* **7**, e35383 (2018).
27. A. Punjani, J. L. Rubinstein, D. J. Fleet, M. A. Brubaker, cryoSPARC: Algorithms for rapid unsupervised cryo-EM structure determination. *Nat. Methods* **14**, 290–296 (2017).
28. S. Q. Zheng, E. Palovcak, J. P. Armache, K. A. Verba, Y. Cheng, D. A. Agard, MotionCor2: Anisotropic correction of beam-induced motion for improved cryo-electron microscopy. *Nat. Methods* **14**, 331–332 (2017).
29. A. Rohou, N. Grigorieff, CTFFIND4: Fast and accurate defocus estimation from electron micrographs. *J. Struct. Biol.* **192**, 216–221 (2015).
30. P. B. Rosenthal, R. Henderson, Optimal determination of particle orientation, absolute hand, and contrast loss in single-particle electron cryomicroscopy. *J. Mol. Biol.* **333**, 721–745 (2003).
31. P. V. Afonine, B. K. Poon, R. J. Read, O. V. Sobolev, T. C. Terwilliger, A. Urzhumtsev, P. D. Adams, Real-space refinement in PHENIX for cryo-EM and crystallography. *Acta Crystallogr. Sect. D Struct. Biol.* **74**, 531–544 (2018).
32. S. Mukherjee, H. Zheng, M. G. Derebe, K. M. Callenberg, C. L. Partch, D. Rollins, D. C. Propheter, J. Rizo, M. Grabe, Q. X. Jiang, L. V. Hooper, Antibacterial membrane attack by a pore-forming intestinal C-type lectin. *Nature* **505**, 103–107 (2014).
33. A. Waterhouse, M. Bertoni, S. Bienert, G. Studer, G. Tauriello, R. Gumienny, F. T. Heer, T. A. P. de Beer, C. Rempfer, L. Bordoli, R. Lepore, T. Schwede, SWISS-MODEL: Homology modelling of protein structures and complexes. *Nucleic Acids Res.* **46**, W296–W303 (2018).
34. P. Emsley, B. Lohkamp, W. G. Scott, K. Cowtan, Features and development of Coot. *Acta Crystallogr. Sect. D Biol. Crystallogr.* **66**, 486–501 (2010).
35. T. I. Croll, ISOLDE: A physically realistic environment for model building into low-resolution electron-density maps. *Acta Crystallogr. Sect. D Struct. Biol.* **74**, 519–530 (2018).
36. C. J. Williams, J. J. Headd, N. W. Moriarty, M. G. Prisant, L. L. Videau, L. N. Deis, V. Verma, D. A. Keedy, B. J. Hintze, V. B. Chen, S. Jain, S. M. Lewis, W. B. Arendall III, J. Snoeyink, P. D. Adams, S. C. Lovell, J. S. Richardson, D. C. Richardson, MolProbity: More and better reference data for improved all-atom structure validation. *Protein Sci.* **27**, 293–315 (2018).
37. T. D. Goddard, C. C. Huang, E. C. Meng, E. F. Pettersen, G. S. Couch, J. H. Morris, T. E. Ferrin, UCSF ChimeraX: Meeting modern challenges in visualization and analysis. *Protein Sci.* **27**, 14–25 (2018).
38. F. Sievers, A. Wilm, D. Dineen, T. J. Gibson, K. Karplus, W. Li, R. Lopez, H. McWilliam, M. Remmert, J. Söding, J. D. Thompson, D. G. Higgins, Fast, scalable generation of high-quality protein multiple sequence alignments using Clustal Omega. *Mol. Syst. Biol.* **7**, 539 (2011).

39. A. M. Waterhouse, J. B. Procter, D. M. A. Martin, M. Clamp, G. J. Barton, Jalview Version 2-A multiple sequence alignment editor and analysis workbench. *Bioinformatics* **25**, 1189–1191 (2009).
40. X. Robert, P. Gouet, Deciphering key features in protein structures with the new ENDscript server. *Nucleic Acids Res.* **42**, W320–W324 (2014).

Acknowledgments: We are grateful to the BMR and RMG Groups (Genentech) for help with construct design and protein expression. We are thankful to I. Kim, A. Gill, and C. Huang for help with protein biochemistry; A. Estevez for help with TEM data collection; and A. Carfi for useful discussions. **Funding:** The Swiss National Science Foundation (SNSF) supports L.P.'s laboratory work (grant number: 310030_204679). **Author contributions:** M.K., L.P., J.P., and C.C. designed the research. M.K., M.C.J., R.S., E.M.G., L.R., C.P.A., R.S., H.H., N.P., C.K., L.C.-A., E.K., A.L.R., and N.M.-M. performed experiments and/or analyzed data. C.C. and M.K. conceived and supervised the project. M.K. and C.C. wrote the manuscript with input from all of the authors. **Competing interests:** M.K., L.R., C.P.A., H.H., M.C.J., L.C.-A., A.L.R., N.M.-M., J.P., and C.C. are Genentech/Roche employees and own shares in the Genentech/Roche group. The other authors declare no competing interests. **Data and materials availability:** All data needed to evaluate the conclusions in the paper are present in the paper and/or the Supplementary Materials. The HCMV Pentamer gHgLUL128-131A bound to Fabs 2C12, 7I13, and 13H11 coordinates and cryo-EM maps were deposited in the PDB: 7T4Q and EMDB: EMD-25685, respectively. The HCMV Pentamer gHgLUL128-131A bound to THBD and Fabs MSL-109 and 13H11 coordinates and cryo-EM maps were deposited in the PDB: 7T4R and EMDB: EMD-25686, respectively. The HCMV Pentamer gHgLUL128-131A bound to NRP2 and Fabs 8I21 and 13H11 coordinates and cryo-EM maps were deposited in the PDB: 7T4S and EMDB: EMD-25687, respectively. The dimeric HCMV Pentamer gHgLUL128-131A bound to NRP2 and Fabs 8I21 and 13H11 cryo-EM maps were deposited in the EMDB: EMD-25688. Requests for materials should be addressed to C.C.

Submitted 3 September 2021
Accepted 25 January 2022
Published 11 March 2022
10.1126/sciadv.abm2536